

# Super-sample covariance of the thermal Sunyaev–Zel’dovich effect

Ken Osato<sup>1,\*</sup> and Masahiro Takada<sup>2</sup>

<sup>1</sup>*Institut d’Astrophysique de Paris, Sorbonne Université, CNRS,  
UMR 7095, 98bis boulevard Arago, 75014 Paris, France*

<sup>2</sup>*Kavli Institute for the Physics and Mathematics of the Universe (WPI),  
The University of Tokyo Institutes for Advanced Study,  
The University of Tokyo, 5-1-5 Kashiwanoha, Kashiwa, 277-8583 Chiba, Japan*

(Dated: February 7, 2022)

The thermal Sunyaev–Zel’dovich (tSZ) effect is a powerful probe of cosmology. The statistical errors in the tSZ power spectrum measurements are dominated by the presence of massive clusters in a survey volume that are easy to identify on individual cluster basis. First, we study the impact of super sample covariance (SSC) on the tSZ power spectrum measurements, and find that the sample variance is dominated by the connected non-Gaussian (cNG) covariance arising mainly from Poisson number fluctuations of massive clusters in the survey volume. Second, we find that removing such individually-detected, massive clusters from the analysis significantly reduces the cNG contribution, thereby leading the SSC to be a leading source of the sample variance. We then show, based on Fisher analysis, that the power spectrum measured from the remaining diffuse tSZ effects can be used to obtain tight constraints on cosmological parameters as well as the hydrostatic mass bias parameter. Our method offers complementary use of individual tSZ cluster counts and the power spectrum measurements of diffuse tSZ signals for cosmology and intracluster gas physics.

## I. INTRODUCTION

The anisotropy of cosmic microwave background (CMB) is one of the most important probes of physical states in the Universe. Among different components of the CMB anisotropy, the Sunyaev–Zel’dovich (SZ) effect [1–3] provides us with rich information of cosmic structures of the late-time Universe (for reviews, see Refs. [4, 5]). The SZ effect is divided into two classes according to physical processes giving rise to the anisotropy. One is the thermal SZ effect (tSZ), where energy is transferred from hot electrons to CMB photons through inverse Compton scattering. The other one is the kinetic SZ effect (kSZ), which is caused by the Doppler effect due to bulk motion of electrons with respect to the rest frame of CMB photons. The tSZ effect arises mainly from thermal electrons, most of which reside in galaxy clusters, and enable one to detect distant galaxy clusters up to high redshifts because the cosmological surface brightness dimming is compensated by the increase of CMB photon number density at higher redshifts. Since the abundance and spatial distribution of galaxy clusters reflect the degree of the structure formation of the Universe, we can take advantage of SZ effects to constrain cosmological parameters [6–10]. Since the amplitude of the tSZ effect is larger than the kSZ effect, and the tSZ effect is easier to be distinguished from other anisotropies due to specific frequency dependence, the tSZ effect has now been intensively studied.

The tSZ effect has already been measured by several survey programs. The *Planck* satellite has conducted the measurement for all-sky coverage [11, 12], and ground-based telescopes aim to measure the tSZ effect with high

angular resolution ( $\sim 1$  arcmin), which includes Atacama Cosmology Telescope (ACT) [13, 14], South Pole Telescope (SPT) [15, 16], Simons Observatory [17], and CMB-S4 [18].

As a summary statistics of the tSZ effect, power spectrum is commonly employed because the theoretical approach is readily available [19]. Among them, the halo model prescription [20–23] can reproduce the results of hydrodynamical simulations [24, 25] and is widely employed in practical analyses [11, 26]. In addition, by cross-correlating the tSZ map with other observables of the large-scale structure, e.g., cosmic shear or nearby galaxies, the significance of the measurements can be enhanced [27–34]. Since the tSZ effect is sourced by hot free electrons and most of them are found in galaxy clusters, i.e., massive halos, the halo model picture is justified. Similarly, we can also estimate the covariance matrix based on the halo model prescription. However, the covariance matrix suffers from large-scale mass fluctuations with wavelengths comparable with or greater than a size of the survey volume, which is not a direct observable. That additional contribution in the covariance is referred to as the super-sample covariance (SSC) [35]. If the SSC contribution is not taken into account, the covariance matrix is underestimated and the statistical significance is overestimated. In order to carry out the analysis with the power spectrum in an unbiased way, we need to incorporate such additional contributions.

In Refs [26, 36], it is shown that the connected non-Gaussian term is a dominant contribution in the covariance of the power spectrum. Furthermore, this term is sourced mainly by massive clusters at low redshifts. Therefore, removing such clusters from the measurement by masking the regions leads to suppression of the covariance matrix and enhancement of the significance though some fraction of signals can be missed [37]. In this pa-

\* ken.osato@iap.fr

per, we estimate the SSC contribution for the tSZ effect based on the halo model prescription and quantify the effects on cosmological parameter estimation with the tSZ power spectrum. Furthermore, we also investigate the effect when massive clusters are masked.

This paper is organized as follows. First, we review the halo model prescription to compute the tSZ power spectrum in Section II and the covariance matrix in Section III. In Section IV, we give specific details on experimental conditions. In Section V, we present results of statistical significance and forecasts of constraints on parameters. We make concluding remarks in Section VI.

Throughout this paper, we assume the flat  $\Lambda$  cold dark matter (CDM) Universe. Otherwise stated, we adopt the best fit cosmological parameters inferred with observations of temperature and polarization anisotropies and gravitational lensing of CMB (TT,TE,EE+lowE+lensing) measured by *Planck* [38, 39]: the physical CDM density  $\Omega_c h^2 = 0.12011$ , the physical baryon density  $\Omega_b h^2 = 0.022383$ , the acoustic angular scale  $100\theta_* = 1.041085$ , the amplitude and slope of the scalar perturbation  $\ln(10^{10} A_s) = 3.0448$ ,  $n_s = 0.96605$  at the pivot scale  $k_{\text{piv}} = 0.05 \text{ Mpc}^{-1}$ , and the optical depth  $\tau_{\text{reio}} = 0.0543$ . The neutrino component is composed of two massless neutrinos and one massive neutrino with the mass  $m_\nu = 0.06 \text{ eV}$ , and the massive neutrino density parameter is  $\Omega_\nu h^2 = m_\nu / (93.14 \text{ eV}) = 0.000644$ . Thus, the matter component is composed of CDM, baryons, and massive neutrinos, and the matter density parameter is  $\Omega_m = \Omega_c + \Omega_b + \Omega_\nu = 0.31816$ . Then, the energy density of cosmological constant is given as  $\Omega_\Lambda = 1 - \Omega_m = 0.68184$ . The amplitude of matter fluctuation at the scale of  $8 h^{-1} \text{ Mpc}$  is  $\sigma_8 = 0.811$ . For notation, the symbol “log” denotes common logarithm “ $\log_{10}$ ” and the symbol “ln” denotes natural logarithm “ $\log_e$ ”.

## II. THE TSZ POWER SPECTRUM

### A. Halo Model of the tSZ Power Spectrum

Here, we briefly review the halo model calculations of the tSZ power spectrum. The temperature variation  $\Delta T$  due to the tSZ effect [1–3] is given by

$$\frac{\Delta T}{T_{\text{CMB}}} = g_\nu(x) y = g_\nu(x) \frac{\sigma_T}{m_e c^2} \int P_e dl, \quad (1)$$

where  $y$  is the Compton- $y$  parameter,  $T_{\text{CMB}} = 2.7255 \text{ K}$  is the CMB temperature,  $\sigma_T$  is the Thomson scattering cross-section,  $m_e$  is the electron mass,  $c$  is the speed of light,  $P_e$  is the free electron pressure, and in the last term, the line-of-sight integration is carried out with respect to the physical length  $l$ . The frequency dependent part  $g_\nu(x)$  is given by

$$g_\nu(x) = x \frac{e^x - 1}{e^x + 1} - 4, \quad x \equiv \frac{h\nu}{k_B T_{\text{CMB}}}, \quad (2)$$

where  $\nu$  is the frequency,  $h$  is the Planck constant, and  $k_B$  is the Boltzmann constant.

First, we give formulations for halo model calculation of the tSZ power spectrum [20, 21]:

$$C(\ell) = C^{1h}(\ell) + C^{2h}(\ell), \quad (3)$$

$$C^{1h}(\ell) = \int_0^{z_{\text{reio}}} d\chi \frac{d^2 V}{d\chi d\Omega} \times \int_{M_{\text{min}}}^{M_{\text{max}}} dM \frac{dn_h}{dM}(M, z) |\tilde{y}(\ell; M, \chi)|^2, \quad (4)$$

$$C^{2h}(\ell) = \int_0^{z_{\text{reio}}} d\chi \frac{d^2 V}{d\chi d\Omega} P_L \left( k = \frac{\ell + 1/2}{\chi}; \chi \right) \times \left[ \int_{M_{\text{min}}}^{M_{\text{max}}} dM \frac{dn_h}{dM}(M, z) b_h(M, z) \tilde{y}(\ell; M, \chi) \right]^2, \quad (5)$$

where  $\chi$  is comoving distance [40],  $d^2 V / d\chi d\Omega = \chi^2$  is the comoving volume per unit comoving distance and unit solid angle,  $dn_h / dM(M, z)$  is the halo mass function,  $P_L(k; \chi)$  is the linear matter power spectrum at redshift  $z$  corresponding to the comoving radial distance  $\chi(z)$ , and  $b_h(M, z)$  is the halo bias. The quantity  $\tilde{y}(\ell; M, \chi)$  is the Fourier transform of the electron pressure profile. The modeling of the pressure profile of halos will be discussed later in this section. The one-halo term (Eq. 4) corresponds to the correlation between the same halo and the two-halo term (Eq. 5) denotes the one between different halos. We assume the reionization occurs instantaneously at  $z_{\text{reio}} = 7$  and at this redshift, all hydrogen and helium are fully ionized. We use the linear Boltzmann code **CLASS** [41] to compute the linear matter power spectrum  $P_L(k, z)$ . In the mass integration, we adopt the virial mass  $M_{\text{vir}}$  as the halo mass definition and employ  $M_{\text{min}} = 10^{11} h^{-1} \text{ M}_\odot$ ,  $M_{\text{max}} = 10^{16} h^{-1} \text{ M}_\odot$  for the lower and upper limits of the halo mass integral, respectively. The virial radius  $R_{\text{vir}}$  for the halo with the virial mass  $M_{\text{vir}}$  is related as follows:

$$M_{\text{vir}} = \frac{4\pi}{3} \Delta_{\text{vir}}(z) \rho_{\text{cr}}(z) R_{\text{vir}}^3, \quad (6)$$

where  $\rho_{\text{cr}}(z)$  is the critical density. The virial overdensity  $\Delta_{\text{vir}}$  is given as [42]

$$\Delta_{\text{vir}} = 18\pi^2 + 82(\Omega_m(z) - 1) - 39(\Omega_m(z) - 1)^2, \quad (7)$$

where

$$\Omega_m(z) = \Omega_m(1+z)^3 E^{-2}(z), \quad (8)$$

and the expansion factor is defined as

$$E(z) = \frac{H(z)}{H_0} = [\Omega_m(1+z)^3 + \Omega_\Lambda]^{\frac{1}{2}}. \quad (9)$$

Since fitting formulas of halo mass function, halo bias, and electron pressure profile adopt halo mass definitions

different from the virial mass, we also use alternative halo mass definitions,  $M_{500}$  and  $M_{200b}$ :

$$M_{500} = \frac{4\pi}{3} 500 \rho_{\text{cr}}(z) R_{500}^3, \quad (10)$$

$$M_{200b} = \frac{4\pi}{3} 200 \rho_{\text{m}}(z) R_{200b}^3, \quad (11)$$

where  $\rho_{\text{m}}(z) = \rho_{\text{cr}}(z) \Omega_{\text{m}}(z)$ . These halo masses can be converted from the virial mass if we assume that the density profile of halos follow Navarro–Frenk–White profile [43, 44]:

$$\rho(r) = \frac{\rho_{\text{s}}}{(r/r_{\text{s}})(1 + r/r_{\text{s}})^2}. \quad (12)$$

The scale density  $\rho_{\text{s}}$  is determined by the relation:

$$M_{\text{vir}} = \int_0^{R_{\text{vir}}} dr 4\pi r^2 \rho(r), \quad (13)$$

and the scale radius  $r_{\text{s}}$  is determined from the mass-concentration relation:

$$c_{\text{vir}}(M_{\text{vir}}, z) = \frac{R_{\text{vir}}}{r_{\text{s}}}, \quad (14)$$

where we adopt the fitting formula calibrated by  $N$ -body simulations in Ref. [45]. In addition, for halo mass function and halo bias, we adopt the fitting formulas calibrated by  $N$ -body simulations: the fitted halo mass function with respect to  $M_{200b}$  in Ref. [46] and the fitted halo bias in Ref. [47].

Next, we derive the expression for the Fourier transform of the Compton- $y$  from a single halo  $\tilde{y}(\ell; M, z)$ :

$$\begin{aligned} \tilde{y}(\ell; M, \chi) &= \frac{4\pi R_{\text{s}}}{\ell_s^2} \frac{\sigma_{\text{T}}}{m_{\text{e}} c^2} \\ &\times \int dx x^2 P_{\text{e}}(x) \frac{\sin((\ell + 1/2)x/\ell_s)}{(\ell + 1/2)x/\ell_s}, \end{aligned} \quad (15)$$

where  $x = r/R_{\text{s}}$ ,  $\ell_s = D_{\text{A}}(\chi)/R_{\text{s}}$ ,  $R_{\text{s}}$  is the arbitrary scale radius,  $D_{\text{A}}(\chi)$  is the angular diameter distance. For pressure profile of free electron, we make use of the universal pressure profile [48] calibrated by *Planck* observations [49]:

$$\frac{P_{\text{e}}(r)}{P_{500}} = p(x) \left[ \frac{M_{500}^{\text{HSE}}}{3 \times 10^{14} h_{70}^{-1} \text{M}_{\odot}} \right]^{0.12}, \quad (16)$$

$$p(x) \equiv \frac{P_0}{(c_{500} x)^{\gamma} [1 + (c_{500} x)^{\alpha}]^{(\beta - \gamma)/\alpha}}, \quad (17)$$

$$\begin{aligned} P_{500} &= 1.65 \times 10^{-3} E(z)^{\frac{8}{3}} \\ &\times \left[ \frac{M_{500}^{\text{HSE}}}{3 \times 10^{14} h_{70}^{-1} \text{M}_{\odot}} \right]^{\frac{2}{3}} h_{70}^2 \text{keV cm}^{-3}, \end{aligned} \quad (18)$$

where  $(P_0, c_{500}, \gamma, \alpha, \beta) = (6.41, 1.81, 0.31, 1.33, 4.13)$ ,  $x = r/R_{500}^{\text{HSE}}$ , and  $h_{70} \equiv h/0.7$ . In the calibration of the pressure profile, the mass is determined with hydrostatic

equilibrium assumption, where only thermal pressure is balanced with the self-gravity of the halo. However, in addition to thermal pressure, non-thermal processes, e.g., turbulence or magnetic field, could also contribute the total pressure supporting the mass of galaxy clusters [50–53]. Thus, the hydrostatic mass  $M_{500}^{\text{HSE}}$  is generally lower than the true mass  $M_{500}$ . In order to take this effect into account, we parametrize the mass and radius with the hydrostatic mass bias parameter  $b_{\text{HSE}}$ :

$$M_{500}^{\text{HSE}} = (1 - b_{\text{HSE}}) M_{500}, \quad (19)$$

$$R_{500}^{\text{HSE}} = (1 - b_{\text{HSE}})^{\frac{1}{3}} R_{500}. \quad (20)$$

We adopt the fiducial value  $b_{\text{HSE}} = 0.2$ , which is suggested by mass calibration measurements [54, 55] and hydrodynamical simulations [56]. The amplitude of the tSZ power spectrum is sensitive to the hydrostatic bias parameter and thus, the parameter can be constrained through the power spectrum in a way complementary to the mass calibration measurements.

## B. Selection Function of Massive Clusters

Here, we introduce an observable in cluster survey relevant for the tSZ effect. For each cluster, the integrated flux of tSZ effect corresponds to the thermal energy stored in the galaxy cluster. We define the three-dimensional integrated Compton- $y$  parameter, which is denoted as  $Y_{500}$ :

$$Y_{500}(M, z) = \frac{\sigma_{\text{T}}}{m_{\text{e}} c^2} \int_0^{R_{500}} dr 4\pi r^2 P_{\text{e}}(r; M, z). \quad (21)$$

This quantity is proportional to the thermal energy of gas in the galaxy cluster and can be measured in the tSZ survey if the redshift of the cluster is known [57]. Furthermore, this quantity exhibits a tight scaling relation with the halo mass [58]. As we will show later, since the dominant source of the tSZ covariance is caused by massive clusters, we study how masking of such massive clusters, based on the integrated Compton- $y$  parameter, helps reduce the sample covariance. We introduce the selection function  $S(M, z)$  based on the integrated Compton- $y$  parameter:

$$S(M, z) = \begin{cases} 1 & (Y_{500}(M, z) \leq Y_{\text{thres}}) \\ 0 & (Y_{500}(M, z) > Y_{\text{thres}}), \end{cases} \quad (22)$$

where  $Y_{\text{thres}}$  is the threshold value. When cluster masking is applied, this selection function is inserted in the mass and redshift integrations in the halo model expressions (see Section III C). In Figure 1, we show how the integrated Compton- $y$  parameter varies with the virial mass and redshift, and the different lines denote three representative values of  $\log(Y_{500}/\text{Mpc}^2) = -6, -5, -4$ . In Figure 2, we show the tSZ power spectrum along with CMB primary spectrum and noise power spectrum,

which will be discussed in Section IV. The tSZ power spectra with and without cluster masking are shown. When cluster masking is applied, the amplitude is suppressed by less than half but the covariance matrix has also been reduced as shown in Section III. Both of one-halo (dashed lines) and two-halo (dot-dashed lines) terms are reduced by cluster masking, but the one-halo term is more suppressed because the main source of the term is nearby massive clusters. As a result, the signal-to-noise ratio is enhanced by masking clusters. We will discuss the statistical significance in Section V A.

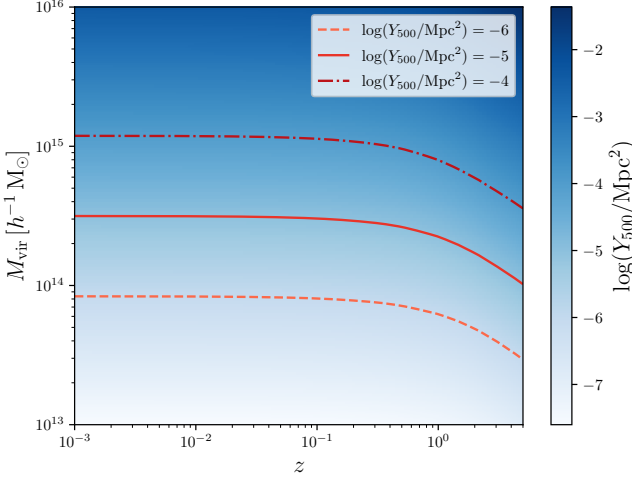


FIG. 1. The integrated Compton- $y$  parameter for clusters of given redshift  $z$  and virial mass  $M_{\text{vir}}$ . The dashed, solid, and dot-dashed lines correspond to  $\log(Y_{500}/\text{Mpc}^2) = -6, -5, -4$ , respectively. For each threshold, clusters located at upper regions divided by the line are masked.

### III. COVARIANCE OF THE TSZ POWER SPECTRUM

#### A. Compton- $y$ with the Survey Mask

Here, we derive formulas of the covariance matrix of the Compton- $y$  power spectrum with taking into account the survey mask. First, we define the survey window function  $W(\boldsymbol{\theta})$  and the observed Compton- $y$  field as

$$y_W(\boldsymbol{\theta}) = W(\boldsymbol{\theta})y(\boldsymbol{\theta}), \quad (23)$$

where  $W(\boldsymbol{\theta}) = 1$  for observed regions and  $W(\boldsymbol{\theta}) = 0$  for masked regions. Then, the Fourier transform of the field under flat-sky approximation is given by

$$\tilde{y}_W(\boldsymbol{\ell}) = \int \frac{d^2\ell'}{(2\pi)^2} \tilde{W}(\boldsymbol{\ell} - \boldsymbol{\ell}') \tilde{y}(\boldsymbol{\ell}'), \quad (24)$$

where the tilde symbol denotes the Fourier transform of the quantity. The estimator of the power spectrum for

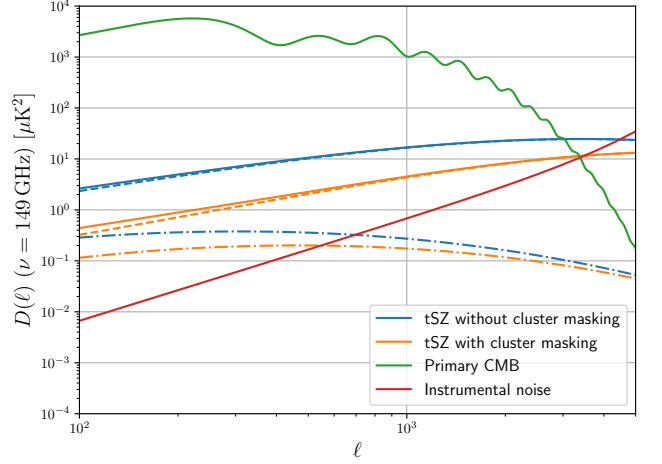


FIG. 2. The power spectra of temperature anisotropy due to the tSZ effect with and without cluster masking. For comparison, the primary CMB anisotropy power spectrum and instrumental noise power spectrum (see Section IV) are also shown. For halo model calculations, the dashed (dot-dashed) lines correspond to one-halo (two-halo) term contribution. Instead of the raw power spectrum  $C(\ell)$ , we show  $D(\ell) = \ell(\ell+1)/(2\pi)C(\ell)$  at the frequency  $\nu = 149$  GHz. For cluster masking, we adopt the threshold  $\log(Y_{\text{thres}}/\text{Mpc}^2) = -5$ .

$i^{\text{th}}$  multipole bin is given as

$$\hat{C}(\ell_i) \equiv \frac{1}{\Omega_W} \int_{\ell \in \ell_i} \frac{d^2\ell}{\Omega_{\ell_i}} \tilde{y}_W(\boldsymbol{\ell}) \tilde{y}_W(-\boldsymbol{\ell}), \quad (25)$$

where  $\Omega_W$  is the effective survey area  $\Omega_W = \int d^2\theta W(\boldsymbol{\theta})$ , and  $\Omega_{\ell_i}$  is the number of modes  $\Omega_{\ell_i} = \int_{\ell \in \ell_i} d^2\ell$ . When the bin width is sufficiently smaller than the multipole, the number of modes can be approximated as

$$\Omega_{\ell_i} \approx 2\pi\ell_i^2 \Delta \ln \ell, \quad (26)$$

where we consider the logarithmically evenly-spaced bins for multipoles and  $\Delta \ln \ell$  is the bin width in logarithmic space. Then, the ensemble average of the estimator becomes the sum of the power spectrum  $C(\ell)$  and noise power spectrum  $N(\ell)$ :

$$\langle \hat{C}(\ell_i) \rangle = C(\ell_i) + N(\ell_i). \quad (27)$$

Hereafter, the parenthesis denotes ensemble average.

#### B. Covariance Matrix of the tSZ Power Spectrum

Next, we derive the expression for the covariance matrix  $\mathcal{C}$  as

$$\begin{aligned} \mathcal{C}_{ij} &\equiv \langle \hat{C}(\ell_i) \hat{C}(\ell_j) \rangle - \langle \hat{C}(\ell_i) \rangle \langle \hat{C}(\ell_j) \rangle \\ &= \frac{1}{\Omega_W} \left[ \frac{(2\pi)^2}{\Omega_{\ell_i}} 2[C(\ell_i) + N(\ell_i)]^2 \delta_{ij} + \bar{T}_W(\ell_i, \ell_j) \right], \end{aligned} \quad (28)$$

where  $\delta_{ij}$  is the Kronecker delta. The first term is referred to as the Gaussian term (labeled as G):

$$C_{ij}^G = \frac{1}{\Omega_W} \frac{(2\pi)^2}{\Omega_{\ell_i}} 2[C(\ell_i) + N(\ell_i)]^2 \delta_{ij}. \quad (29)$$

The remaining term is the non-Gaussian term, which does not depend on the binning of the multipoles in contrast to the Gaussian term. The trispectrum convoluted with the window function  $\bar{T}_W$  is given as

---


$$\bar{T}_W(\ell_i, \ell_j) = \frac{1}{\Omega_W} \int_{l \in \ell_i} \frac{d^2 \ell}{\Omega_{\ell_i}} \int_{l \in \ell_j} \frac{d^2 \ell'}{\Omega_{\ell_j}} \int \left[ \prod_{a=1}^4 \frac{d^2 q_a}{(2\pi)^2} \tilde{W}(\mathbf{q}_a) \right] (2\pi)^2 \delta_D(\mathbf{q}_{1234}) T(\ell + \mathbf{q}_1, -\ell + \mathbf{q}_2, \ell' + \mathbf{q}_3, -\ell' + \mathbf{q}_4), \quad (30)$$


---

where  $\delta_D$  is the Dirac delta function and  $\mathbf{q}_{1234} \equiv \mathbf{q}_1 + \mathbf{q}_2 + \mathbf{q}_3 + \mathbf{q}_4$ .

Then, we derive the expressions of the covariance matrix based on halo model [59]. First, we introduce the following notation:

$$I_\mu^\beta(\ell_1, \dots, \ell_\mu; \chi) \equiv \int dM \frac{dn_h}{dM} b_\beta \tilde{y}(\ell_1) \cdots \tilde{y}(\ell_\mu), \quad (31)$$

where  $b_0 = 1$  and  $b_1 = b_h(M, z)$ . The halo model expres-

---

sion of the tSZ power spectrum becomes

$$C(\ell) = \int d\chi \frac{d^2 V}{d\chi d\Omega} \left[ I_2^0(\ell, \ell; \chi) + [I_1^1(\ell; \chi)]^2 \times P_L \left( k = \frac{\ell + 1/2}{\chi}, \chi \right) \right]. \quad (32)$$

For projected fields such as Compton- $y$ , we can compute the non-Gaussian terms for covariance as follows [8, 60, 61]:

$$C_{ij}^{\text{NG}} = C_{ij}^{\text{cNG}} + C_{ij}^{\text{SSC}}, \quad (33)$$

$$C_{ij}^{\text{cNG}} = \frac{1}{\Omega_W} \int_{l \in \ell_i} \frac{d^2 \ell}{\Omega_{\ell_i}} \int_{l \in \ell_j} \frac{d^2 \ell'}{\Omega_{\ell_j}} T(\ell, -\ell, \ell', -\ell'), \quad (34)$$

$$C_{ij}^{\text{SSC}} = C_{ij}^{\text{HSV}} + C_{ij}^{\text{HSV-BC}} + C_{ij}^{\text{BC}}, \quad (35)$$

$$\begin{aligned} C_{ij}^{\text{HSV}} &= \int d\chi \frac{d^2 V}{d\chi d\Omega} I_2^1(\ell_i, \ell_i; \chi) I_2^1(\ell_j, \ell_j; \chi) \frac{1}{\Omega_W^2} \int \frac{d^2 \ell}{(2\pi)^2} |\tilde{W}(\ell)|^2 P_L(k; \chi) \\ &= \int d\chi \frac{d^2 V}{d\chi d\Omega} I_2^1(\ell_i, \ell_i; \chi) I_2^1(\ell_j, \ell_j; \chi) [\sigma_W^L(\chi)]^2, \end{aligned} \quad (36)$$

$$C_{ij}^{\text{BC}} = \int d\chi \frac{d^2 V}{d\chi d\Omega} \left( \frac{68}{21} \right)^2 [I_1^1(\ell_i; \chi) I_1^1(\ell_j; \chi)]^2 P_L(k_i; \chi) P_L(k_j; \chi) [\sigma_W^L(\chi)]^2, \quad (37)$$

$$C_{ij}^{\text{HSV-BC}} = \int d\chi \frac{d^2 V}{d\chi d\Omega} \frac{68}{21} \{ [I_1^1(\ell_i; \chi)]^2 I_2^1(\ell_j, \ell_j; \chi) P_L(k_i; \chi) + [I_1^1(\ell_j; \chi)]^2 I_2^1(\ell_i, \ell_i; \chi) P_L(k_j; \chi) \} [\sigma_W^L(\chi)]^2, \quad (38)$$


---

where we define the variance of mass density fluctuations of super-survey modes as

$$[\sigma_W^L(\chi)]^2 \equiv \frac{1}{\Omega_W^2} \int \frac{d^2 \ell}{(2\pi)^2} |\tilde{W}(\ell)|^2 P_L(k; \chi), \quad (39)$$

and  $k \equiv (\ell + 1/2)/\chi$ . The term which is sourced from the trispectrum with parallelogram configuration is re-

ferred to as the connected non-Gaussian term (labeled as cNG). The latter three terms are referred to as the halo sample variance [61, HSV] the beat coupling [60, 62, BC] and their cross-correlation (HSV-BC) terms, respectively. The sum of the three terms is referred to as super sample variance [35, SSC]. Since the trispectrum is dominated by the one-halo term at all scales [59], we ignore

the two-, three-, and four-halo terms of the trispectrum for simplicity:

$$\begin{aligned} T(\ell, -\ell, \ell', -\ell') &\approx T^{1h}(\ell, \ell') \\ &= \int d\chi \frac{d^2V}{d\chi d\Omega} \int dM \frac{dn_h}{dM} \\ &\quad \times |\tilde{y}(\ell; M, \chi)|^2 |\tilde{y}(\ell'; M, \chi)|^2. \end{aligned} \quad (40)$$

### C. Implementation of Cluster Masking in Halo Model

Here, we describe how to incorporate the cluster masking in the halo model expressions of tSZ power spectrum and covariance matrix. The selection function  $S(M, \chi)$  (Eq. 22) is inserted in the mass integration in  $I_\mu^\beta$  and  $T^{1h}$ :

$$\begin{aligned} I_\mu^\beta(\ell_1, \dots, \ell_\mu; \chi) &\rightarrow \hat{I}_\mu^\beta(\ell_1, \dots, \ell_\mu; \chi) \\ &\equiv \int dM \frac{dn_h}{dM} S(M, \chi) b_\beta \tilde{y}(\ell_1) \cdots \tilde{y}(\ell_\mu), \end{aligned} \quad (41)$$

and

$$\begin{aligned} T^{1h}(\ell, \ell') &\rightarrow \hat{T}^{1h}(\ell, \ell') \\ &\equiv \int d\chi \frac{d^2V}{d\chi d\Omega} \int dM \frac{dn_h}{dM} S(M, \chi) \\ &\quad \times |\tilde{y}(\ell; M, \chi)|^2 |\tilde{y}(\ell'; M, \chi)|^2. \end{aligned} \quad (42)$$

Then, in order to apply cluster masking,  $I_\mu^\beta$  and  $T^{1h}$  in halo model expressions (Eqs. 32, 34, 36, 37, and 38) are replaced with  $\hat{I}_\mu^\beta$  and  $\hat{T}^{1h}$ , respectively.

### D. Weight Function

In order to investigate which halos contribute the signal and covariance, we compute the weight function with respect to mass and redshift. For the power spectrum, the weight function is given as

$$\begin{aligned} \frac{d^2}{dz dM} C(\ell) &= \frac{d^2V}{dz d\Omega} \left[ \frac{dn_h}{dM} |\tilde{y}(\ell)|^2 + 2 \frac{dn_h}{dM} b_h \tilde{y}(\ell) \right. \\ &\quad \left. \times P_L \left( k = \frac{\ell + 1/2}{\chi}, z \right) \int dM \frac{dn_h}{dM} b_h \tilde{y}(\ell) \right]. \end{aligned} \quad (43)$$

Similarly, the weight function of the trispectrum is given as

$$\begin{aligned} \frac{d^2}{dz dM} T(\ell, -\ell, \ell', -\ell') &\approx \frac{d^2}{dz dM} T^{1h}(\ell, \ell') \\ &= \frac{d^2V}{dz d\Omega} \frac{dn_h}{dM} |\tilde{y}(\ell)|^2 |\tilde{y}(\ell')|^2. \end{aligned} \quad (44)$$

Note that these expressions are weight functions with respect to the redshift  $z$ , instead of the comoving distance

$\chi$ , and the comoving volume with respect to redshift is  $d^2V/dz d\Omega = \chi^2(z)H(z)/c$ .

Figure 3 shows the weight functions for diagonal components, i.e.,  $\ell = \ell'$  of power spectrum and trispectrum for three representative multipoles  $\ell = 100, 1000, 5000$ . Obviously, the trispectrum is more sensitive to massive clusters than power spectrum at all scales. The integrand of mass integration of trispectrum contains  $\tilde{y}^4$  in contrast to  $\tilde{y}^2$  at highest for power spectrum, and thus, the contribution from massive clusters becomes prominent in trispectrum. Similarly, we can expect that the super-sample covariance involves the mass integration of  $\tilde{y}^2$  at highest and is less sensitive to massive clusters compared with the cNG term. We also show the three critical lines of  $\log(Y_{500}/\text{Mpc}^2) = -6$  (dashed),  $-5$  (solid),  $-4$  (dot-dashed). In order to enhance the significance of the detection, we need to keep the power spectrum but remove the trispectrum contribution as much as possible, which is the dominant source of the covariance. We adopt the fiducial threshold as  $\log(Y_{\text{thres}}/\text{Mpc}^2) = -5$  when masking massive clusters. Apparently, the threshold  $\log(Y_{\text{thres}}/\text{Mpc}^2) = -4$  keeps the large fraction of the signal but our fiducial threshold gives higher significance. Since the contribution of the cNG term is quite larger than other terms, rather than maintaining the signal, completely excluding the trispectrum is a more effective strategy.

## IV. EXPERIMENTAL CONDITIONS

In this Section, we define the experimental conditions for statistical analysis. We consider a practical case which is similar to Advanced ACT measurement [63]. We assume the sky coverage is  $\Omega_W = 2100 \text{ deg}^2$  and the survey window is circular symmetric for simplicity. The power spectrum of the mask is given as

$$|\tilde{W}(\ell)|^2 = \Omega_W^2 \left[ 2 \frac{J_1(\ell \Theta_W)}{\ell \Theta_W} \right]^2, \quad (45)$$

where  $J_1(x)$  is the first-order Bessel function and we employ  $\Theta_W \equiv \sqrt{\Omega_W/\pi}$ . In general, the survey window function has irregular shape or the survey regions are divided into multiple separate patches. The relative strength of SSC depends on the geometry of the survey region or the degree of discontinuity of survey regions [64]. The compact survey geometry such as a circular geometry considered here has the largest SSC contribution. Hence the following estimate can be considered as the worst case scenario of the impact of SSC contribution. The binning is logarithmically evenly spaced with the minimum  $\ell_{\min} = 100$ , the maximum  $\ell_{\max} = 5000$ , and the number of bins  $n_\ell = 30$ . For the noise power spectrum, we assume the instrumental noise is Gaussian and its variance is  $\sigma_{\text{inst}} = 7 \mu\text{K arcmin}$  with the single band at  $\nu_0 = 149 \text{ GHz}$ . Then, the noise power spectrum

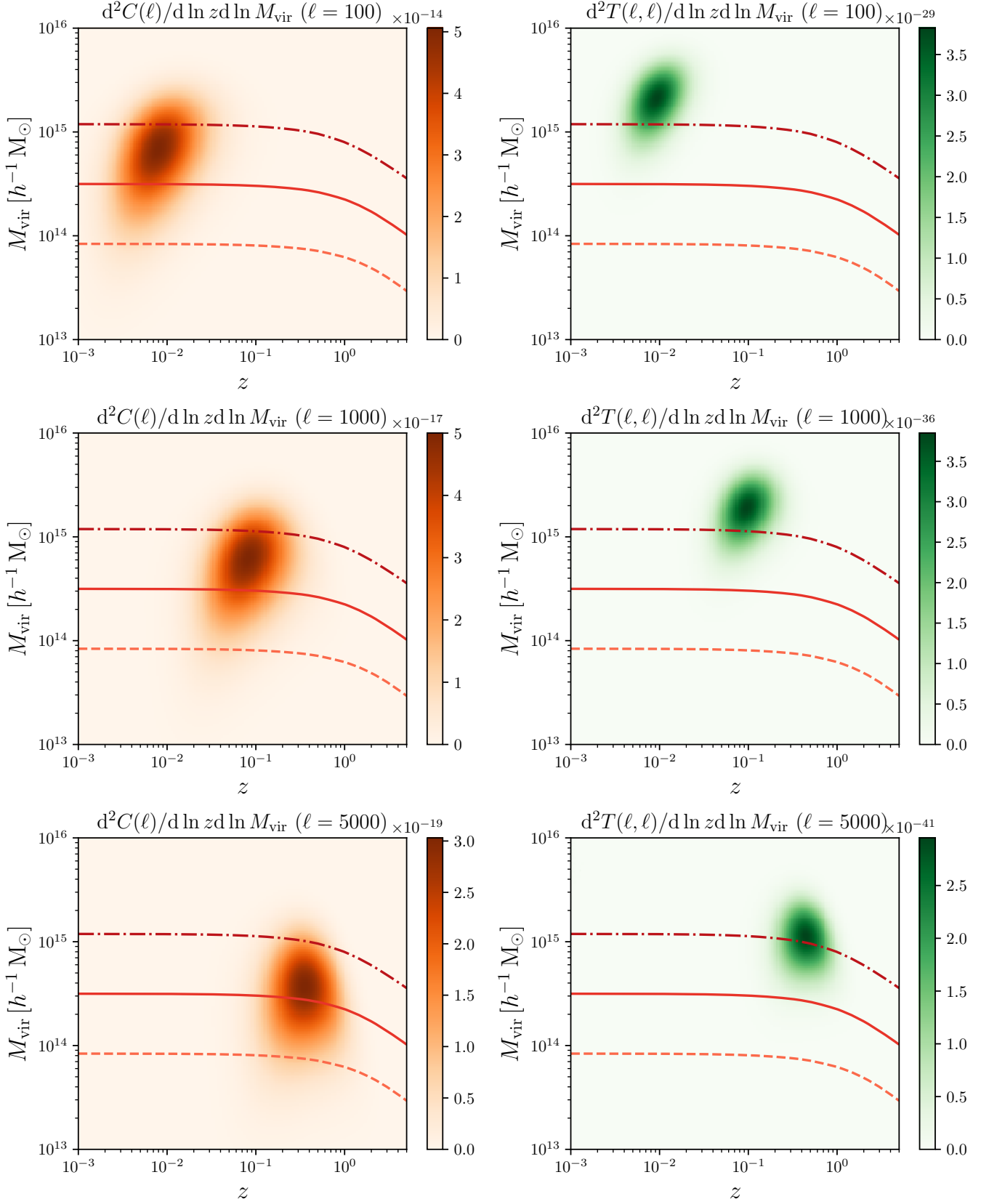


FIG. 3. The differential contributions of clusters in infinitesimal intervals of redshift and halo mass around given redshift ( $x$ -axis) and mass ( $y$ -axis) to the power spectrum and the diagonal term of trispectrum for  $\ell = 100$  (upper panels), 1000 (medium panels), 5000 (lower panels), respectively. The dashed, solid, and dot-dashed lines correspond to  $\log(Y_{500}/\text{Mpc}^2) = -6, -5, -4$ , respectively.

is given as

$$N(\ell) = \left[ \frac{\sigma_{\text{inst}}}{g(\nu_0)T_{\text{CMB}}} \right]^2 e^{\ell^2 \theta_{\text{FWHM}}^2 / (8 \ln 2)}, \quad (46)$$

where  $\theta_{\text{FWHM}} = 1.4$  arcmin is the full width at half maximum of the beam size [63]. In addition to the instrumental noise, radio and infrared point sources, cosmic infrared background, and primary CMB leak to Compton- $y$  estimates due to incomplete separation and can be a source of noise. However, the instrumental noise dominates at small scales [19, 26], and we ignore the contributions from other sources in the subsequent analyses for simplicity. The total covariance matrix is shown in Figure 4. The diagonal term of the covariance matrix for each component is shown in Figure 5. In the case of no cluster masking, the cNG term dominates at all scales. On the other hand, cluster masking removes clusters which contribute to the cNG term, and Gaussian and SSC terms become important when clusters are masked.

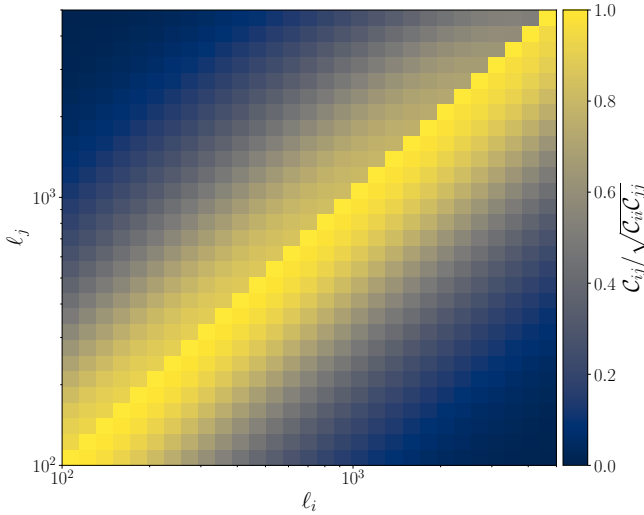


FIG. 4. The total covariance matrix of the tSZ power spectrum. The upper left (lower right) part corresponds to the covariance matrix with (without) cluster masking.

## V. RESULTS

### A. Statistical Significance

In this section, we discuss the statistical significance of the detection of the tSZ power spectrum and the effects of cluster masking and SSC on it. The signal-to-noise ratio (SNR)  $S/N$  is computed as

$$\frac{S}{N} = \left[ \sum_{\ell_{\min} \leq \ell_i, \ell_j \leq \ell_{\max}} C(\ell_i) C_{ij}^{-1} C(\ell_j) \right]^{\frac{1}{2}}. \quad (47)$$

Figure 6 shows the SNR as a function of the maximum multipole  $\ell_{\max}$ . The SSC contributes to only 5% of the SNR without cluster masking because the cNG term dominates. However, by masking massive clusters, the overall SNR is enhanced due to the suppression of the cNG term but the relative contribution from SSC also rises up to 30% because the SSC is less sensitive to the cluster masking.

Next, we discuss how SSC affects the chi-square statistic that an observer could obtain for a given realization of data. The chi-square statistic is defined as

$$\chi^2 \equiv (\mathbf{d} - \bar{\mathbf{d}})^T \mathbf{C}^{-1} (\mathbf{d} - \bar{\mathbf{d}}), \quad (48)$$

where  $\mathbf{d}$  is the data vector defined as

$$\mathbf{d} = (C(\ell_1), \dots, C(\ell_{n_\ell})), \quad (49)$$

and  $\bar{\mathbf{d}} \equiv \langle \mathbf{d} \rangle$ . The expectation value of the  $\chi^2$  value is estimated as

$$\begin{aligned} \langle \chi^2 \rangle &= \langle (\mathbf{d} - \bar{\mathbf{d}})^T \mathbf{C}^{-1} (\mathbf{d} - \bar{\mathbf{d}}) \rangle \\ &= \text{Tr}(\langle (\mathbf{d} - \bar{\mathbf{d}})(\mathbf{d} - \bar{\mathbf{d}})^T \rangle \mathbf{C}^{-1}) \\ &= \text{Tr}(\mathbf{C} \mathbf{C}^{-1}) = n_\ell. \end{aligned} \quad (50)$$

However, if the wrong covariance is employed in the analysis, the expected chi-square deviates from the number of bins. Let us consider the case where the true covariance is composed of Gaussian, connected non-Gaussian, and super-sample covariance, and the wrong covariance is that without the super-sample covariance:

$$\mathbf{C}_{\text{true}} \equiv \mathbf{C}^G + \mathbf{C}^{\text{cNG}} + \mathbf{C}^{\text{SSC}}, \quad (51)$$

$$\mathbf{C}_{\text{wrong}} \equiv \mathbf{C}^G + \mathbf{C}^{\text{cNG}}. \quad (52)$$

Then, the expectation value of chi-square with the wrong covariance is given as

$$\begin{aligned} \langle \chi_{\text{wrong}}^2 \rangle &= \langle (\mathbf{d} - \bar{\mathbf{d}})^T (\mathbf{C}_{\text{wrong}})^{-1} (\mathbf{d} - \bar{\mathbf{d}}) \rangle \\ &= \text{Tr}(\mathbf{C}_{\text{true}} (\mathbf{C}_{\text{wrong}})^{-1}) > n_\ell. \end{aligned} \quad (53)$$

The chi-square with the wrong covariance no longer follows the chi-squared distribution but if the wrong covariance is close to the true covariance, we can approximate the probability distribution function (PDF) of  $\chi_{\text{wrong}}^2$  as the chi-squared distribution with scaling to match the expectation value:

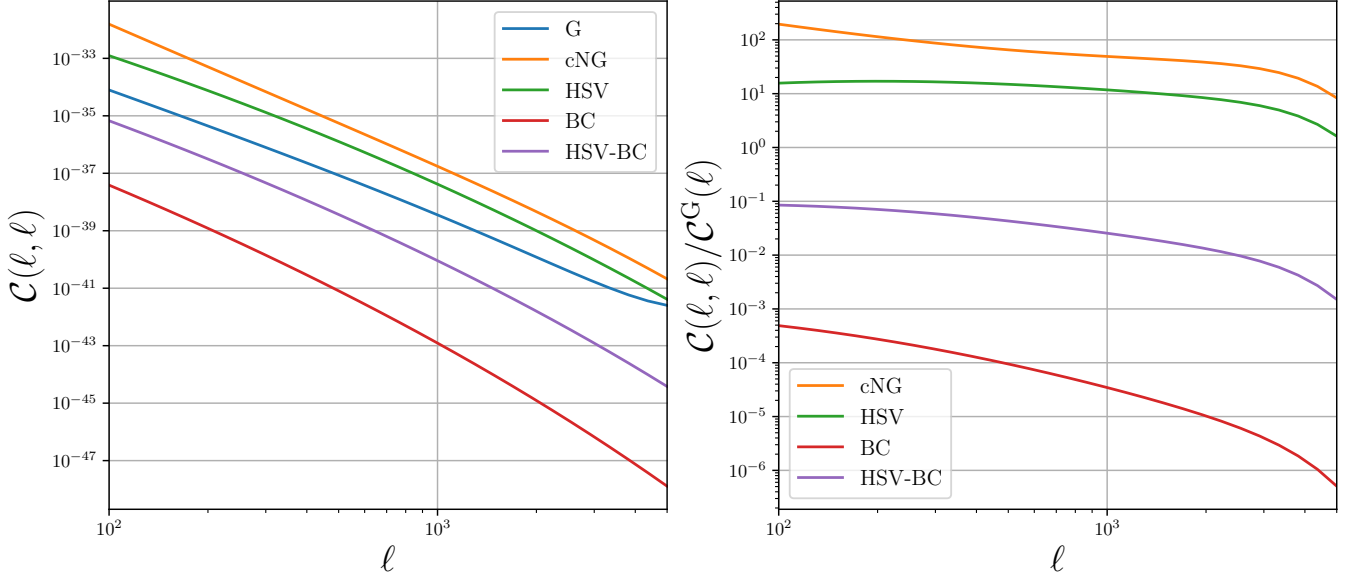
$$P(\chi_{\text{wrong}}^2) d\chi_{\text{wrong}}^2 \approx P_{\chi^2} \left( \frac{n_\ell}{\alpha} \chi_{\text{wrong}}^2; n_\ell \right) \frac{n_\ell}{\alpha} d\chi_{\text{wrong}}^2, \quad (54)$$

where  $P_{\chi^2}(\chi^2; n)$  is PDF of chi-squared distribution with the degree of freedom  $n$ , and  $\alpha \equiv \text{Tr}(\mathbf{C}_{\text{true}} (\mathbf{C}_{\text{wrong}})^{-1})$ .

Figure 7 shows the PDFs with the true covariance and the wrong ones, i.e., without SSC, for the cases with and without cluster masking. The PDFs with wrong covariances are skewed rightward compared with the true one because the wrong covariance underestimates the true covariance or more exactly the amplitude of statistical



## Without cluster masking



## With cluster masking

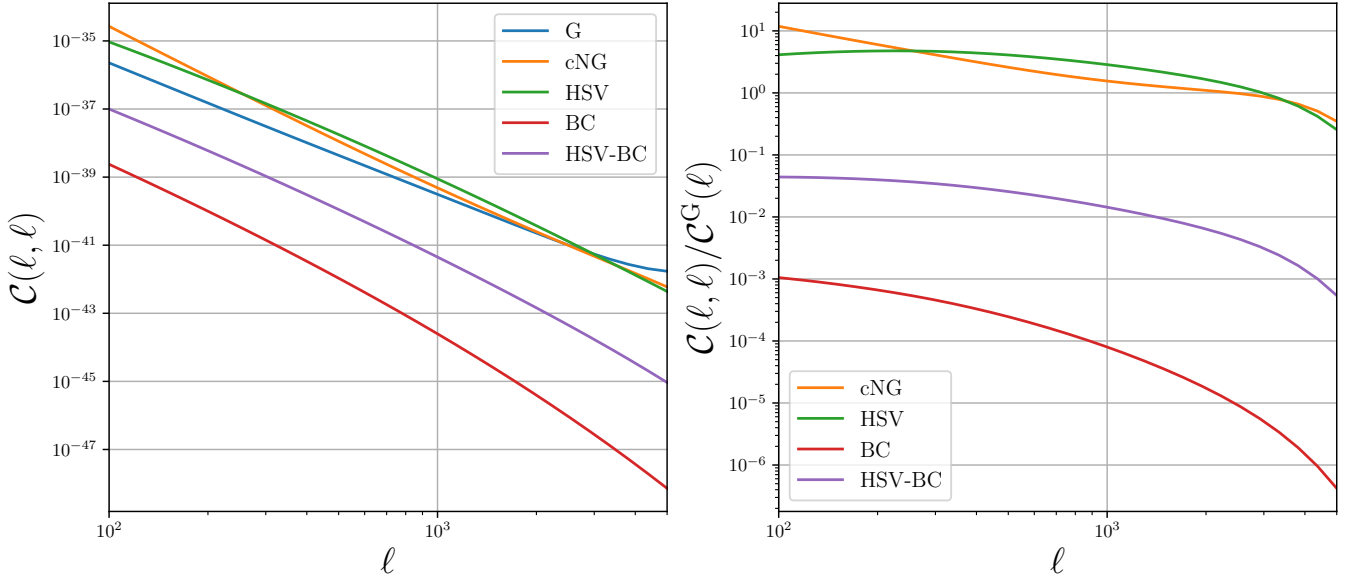


FIG. 5. The diagonal terms of the covariance matrix of the tSZ power spectrum (left panels) and each term divided by the Gaussian term (right panels) without (upper panels) and with (lower panels) cluster masking. The HSV, BC, and HSV-BC terms correspond to the SSC.

scatters, and it apparently gives a higher significance. In order to see how the significance is overestimated with the wrong covariance, we address how the  $p$ -value changes. First, we compute the  $\chi^2_{p=0.05}$ , which gives the  $p$ -value as 0.05 with the true covariance. When the true covariance is adopted, the resultant chi-square follows the chi-squared distribution and from the cumulative distribution function,  $\chi^2_{p=0.05} = 43.8$  is calculated. Then, we

compute the  $p$ -values with wrong covariances, i.e.,

$$p = \int_{\chi^2_{p=0.05}}^{\infty} P(\chi^2_{\text{wrong}}) d\chi^2_{\text{wrong}}. \quad (55)$$

In Table I, we show the  $p$ -values for the two cases with and without cluster masking. When cluster masking is not applied, the effect of the super-sample covariance is subdominant and the  $p$ -value increases only by 1.1%.

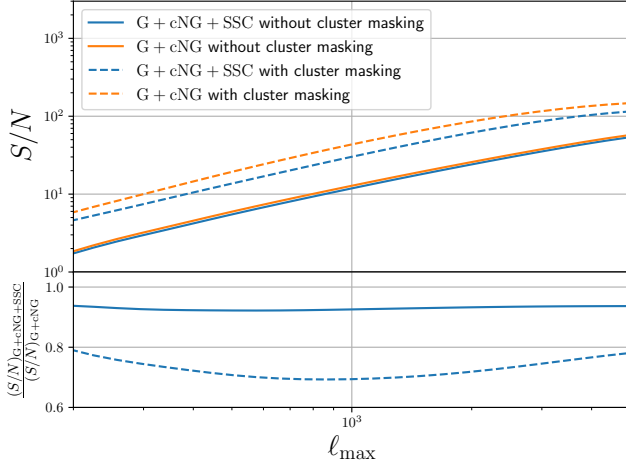


FIG. 6. The SNR as a function of maximum multipole  $\ell_{\max}$  with the total covariance including SSC or the covariance including only the Gaussian and trispectrum (cNG) contributions (i.e. without SSC), as denoted in the legend. The lowest multipole is fixed as  $\ell_{\min} = 100$  and the highest multipole is varied in the range of  $200 \leq \ell_{\max} \leq 5000$ . The bin width is also fixed. The lower panel shows the ratio of  $S/N$  values with and without the SSC contribution, for the two cases where we remove massive clusters with  $Y_{500} > 10^{-5} \text{ Mpc}^{-2}$  or not (with and without “cluster masking”).

Covariance	$\langle \chi^2 \rangle$	$p$ -value
True covariance	30	0.05
Wrong covariance without cluster masking	30.80	0.061
Wrong covariance with cluster masking	33.91	0.120

TABLE I. The  $p$ -values with wrong covariances with and without cluster masking. The lower limit of chi-square is determined as the  $p$ -value with the true covariance is 0.05.

However, when massive clusters are masked, the SSC becomes relatively important and the  $p$ -value is 12.0%. This result implies that it is 7.0% more likely to derive optimistic significance of the detection. Or for a case of parameter inference, even a true model gives an apparent bad fitting to the data, because there might be a higher chance to have a relatively large chi-square value for the best-fit model due to the underestimation in the covariance amplitude.

## B. Fisher Analysis

In this Section, we quantify the effects of SSC on the parameter constraints with tSZ power spectrum based on Fisher forecast [65, 66]. The tSZ power spectrum is sensitive to the matter fluctuation and has potential to place tight constraints on the amplitude  $A_s$ . Furthermore, the hydrostatic mass bias parameter can also be constrained, which information is not accessible solely

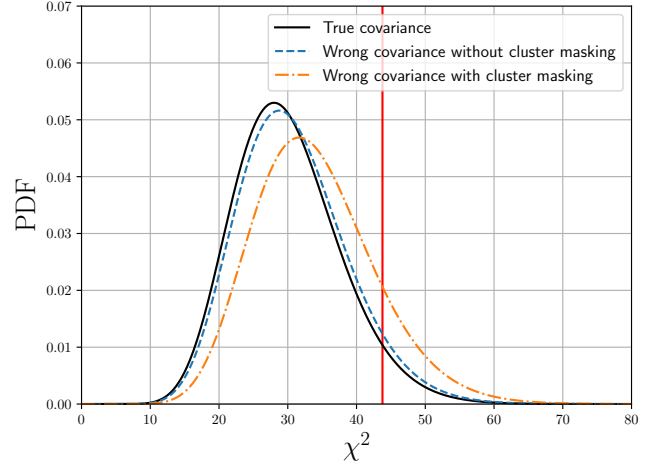


FIG. 7. The PDFs of chi-square with true and wrong covariances and with and without cluster masking. The black solid line shows the chi-square distribution with degree of freedom  $n = 30$  and for the other lines, the argument is scaled to match the expectation values. The blue dashed line shows the PDF with the wrong covariance, i.e., without the SSC term, and furthermore, the orange dot-dashed line shows the one when massive clusters are masked. The red vertical line corresponds to  $\chi^2 = 43.8$  where the  $p$ -value is 0.05 with the true covariance.

from CMB temperature and polarization analysis.

When the likelihood is assumed to be multi-variate Gaussian, the Fisher matrix is given as

$$F_{ij}^{\text{tSZ}} = \frac{\partial \mathbf{d}^T}{\partial \theta_i} \mathbf{C}^{-1} \frac{\partial \mathbf{d}}{\partial \theta_j} + \frac{1}{2} \text{Tr} \left( \mathbf{C}^{-1} \frac{\partial \mathbf{C}}{\partial \theta_i} \mathbf{C}^{-1} \frac{\partial \mathbf{C}}{\partial \theta_j} \right). \quad (56)$$

We consider the parameter space  $\boldsymbol{\theta} = (\Omega_b h^2, \Omega_c h^2, 100\theta_*, \ln(10^{10} A_s), n_s, \tau_{\text{reio}}, B)$ , where  $B = (1 - b_{\text{HSE}})^{-1}$ . In particular, the hydrostatic bias parameter  $B$  characterizes the non-thermal pressure support of galaxy clusters and groups, and it is not well constrained compared with cosmological parameters. Since only with the tSZ power spectrum, severe degeneracy between parameters occurs, we add information from *Planck* 2018 TT, TE, EE+lowE+lensing result [39]. Thus, the resultant Fisher matrix  $F$  is given by

$$F = F^{\text{tSZ}} + F^{\text{CMB}}, \quad (57)$$

where the Fisher matrix for CMB anisotropies are computed from obtained chains in *Planck* analysis. In Figures 8 and 9, forecasts of the constraints from tSZ power spectrum and CMB anisotropies with and without cluster masking are shown. Table II shows the forecast of  $1\text{-}\sigma$  errors. When adding the information of the tSZ power spectrum, we can obtain tighter constraints on parameters, especially the amplitude of primordial curvature perturbations:  $\ln(10^{10} A_s)$ . Note that the hydrostatic bias parameter  $B$  can also be tightly constrained. When clusters are not masked, the effect of SSC is subdominant

since the cNG term is much larger. On the other hand, with cluster masking, the SSC comes into effect because the SSC is not sensitive to cluster masking compared with the cNG term. As the SNR improves by cluster masking, the constraints become tighter.

## VI. CONCLUSIONS

The tSZ effect is one of the most important probes in cosmology. With the power spectrum, we can constrain the cosmological parameters and investigate the astrophysical effects, e.g., hydrostatic mass bias. Since any survey is done for a finite volume, even for a full-sky survey, it is important to realize the impact of the super-survey modes on the statistical power of tSZ power spectrum. We quantify the contribution based on the halo model approach and address biases in parameter estimation. However, it is found that the super-survey covariance is subdominant compared with the cNG term, which is sourced from the trispectrum with the parallelogram configuration.

In order to enhance the statistical significance, it is proposed that massive nearby galaxy clusters, which are dominant source of trispectrum, should be masked to suppress the contribution of the cNG term [37]. We propose the cluster masking based on integrated Compton- $y$  parameter, which corresponds to the thermal energy content in galaxy clusters, and the method enables one to significantly reduces the cNG term. On the other hand, even after masking clusters, the SSC remains because it originates from relatively less massive clusters similarly to the power spectrum signal. Though the overall statistical significance improves, the SSC has appreciable effect and weakens the constraints on the parameters.

We have carried out Fisher forecasts on cosmological parameters and hydrostatic mass bias parameter through the tSZ power spectrum measurement combining with the results of *Planck* CMB anisotropy measure-

ments. In particular, the hydrostatic mass bias parameter, which cannot be constrained only with primary CMB anisotropies, can be tightly constrained through the tSZ power spectrum. By masking clusters, the constraints on the parameters related to the primordial power spectrum, i.e.,  $A_s$  and  $n_s$ , and the hydrostatic mass bias parameter improve. On the other hand, the SSC becomes important because it persists after masking. For example, the constraint on the hydrostatic mass bias with covariance including SSC is 10% larger than that with covariance excluding SSC. Since the effect of SSC remains at all scales, it is critical to incorporate the SSC for accurate estimates on parameters both for ongoing and upcoming observational surveys of the tSZ effect. Moreover, the cluster masking loses the information from massive galaxy clusters. In order to compensate for the loss, the joint analysis with cluster counts is thought to be a practical solution [9, 67, 68]. The method we developed in this paper increases the potential of tSZ cosmology. Massive clusters with significant tSZ signals on individual cluster basis can be used for cosmology, e.g. via the number counts of the clusters. On the other hand, when those clusters are masked from the power spectrum measurement, the tSZ power spectrum can be used to estimate the cosmological parameters. Thus, we showed that massive clusters and other tSZ clusters can play complementary roles to cosmology. This direction is worth further exploring in more detail.

## ACKNOWLEDGMENTS

K.O. is supported by JSPS Overseas Research Fellowships. This work is also supported in part by the World Premier International Research Center Initiative (WPI Initiative), MEXT, Japan, Reischauer Institute of Japanese Studies at Harvard University, and JSPS KAKENHI Grant Numbers JP15H05887, JP15H05893, JP15H05896, JP15K21733, and JP19H00677.

- 
- [1] R. A. Sunyaev and Y. B. Zel'dovich, *Astrophys. Space Sci.* **7**, 3 (1970).
  - [2] R. A. Sunyaev and Y. B. Zel'dovich, *Comments on Astrophysics and Space Physics* **4**, 173 (1972).
  - [3] R. A. Sunyaev and Y. B. Zel'dovich, *Mon. Not. Roy. Astron. Soc.* **190**, 413 (1980).
  - [4] J. E. Carlstrom, G. P. Holder, and E. D. Reese, *Annu. Rev. Astron. Astrophys.* **40**, 643 (2002), arXiv:astro-ph/0208192 [astro-ph].
  - [5] T. Kitayama, *Progress of Theoretical and Experimental Physics* **2014**, 06B111 (2014), arXiv:1404.0870 [astro-ph.CO].
  - [6] Z. Haiman, J. J. Mohr, and G. P. Holder, *Astrophys. J.* **553**, 545 (2001), arXiv:astro-ph/0002336 [astro-ph].
  - [7] E. Komatsu and U. Seljak, *Mon. Not. Roy. Astron. Soc.* **336**, 1256 (2002), arXiv:astro-ph/0205468 [astro-ph].
  - [8] M. Takada and S. Bridle, *New Journal of Physics* **9**, 446 (2007), arXiv:0705.0163 [astro-ph].
  - [9] M. Oguri and M. Takada, *Phys. Rev. D* **83**, 023008 (2011), arXiv:1010.0744 [astro-ph.CO].
  - [10] L. Salvati, M. Douspis, and N. Aghanim, *Astron. Astrophys.* **614**, A13 (2018), arXiv:1708.00697 [astro-ph.CO].
  - [11] Planck Collaboration, *Astron. Astrophys.* **594**, A22 (2016), arXiv:1502.01596 [astro-ph.CO].
  - [12] Planck Collaboration, *Astron. Astrophys.* **594**, A24 (2016), arXiv:1502.01597 [astro-ph.CO].
  - [13] D. S. Swetz, P. A. R. Ade, M. Amiri, J. W. Appel, E. S. Battistelli, B. Burger, J. Chervenak, M. J. Devlin, S. R. Dicker, W. B. Doriese, R. Dünner, T. Essinger-Hileman, R. P. Fisher, J. W. Fowler, M. Halpern, M. Hasselfield, G. C. Hilton, A. D. Hincks, K. D. Irwin, N. Jarosik, M. Kaul, J. Klein, J. M. Lau, M. Limon, T. A. Marriage, D. Marsden, K. Martocci, P. Mauskopf, H. Moseley, C. B. Netterfield, M. D. Niemack, M. R. Nolte, L. A.

# Without cluster masking

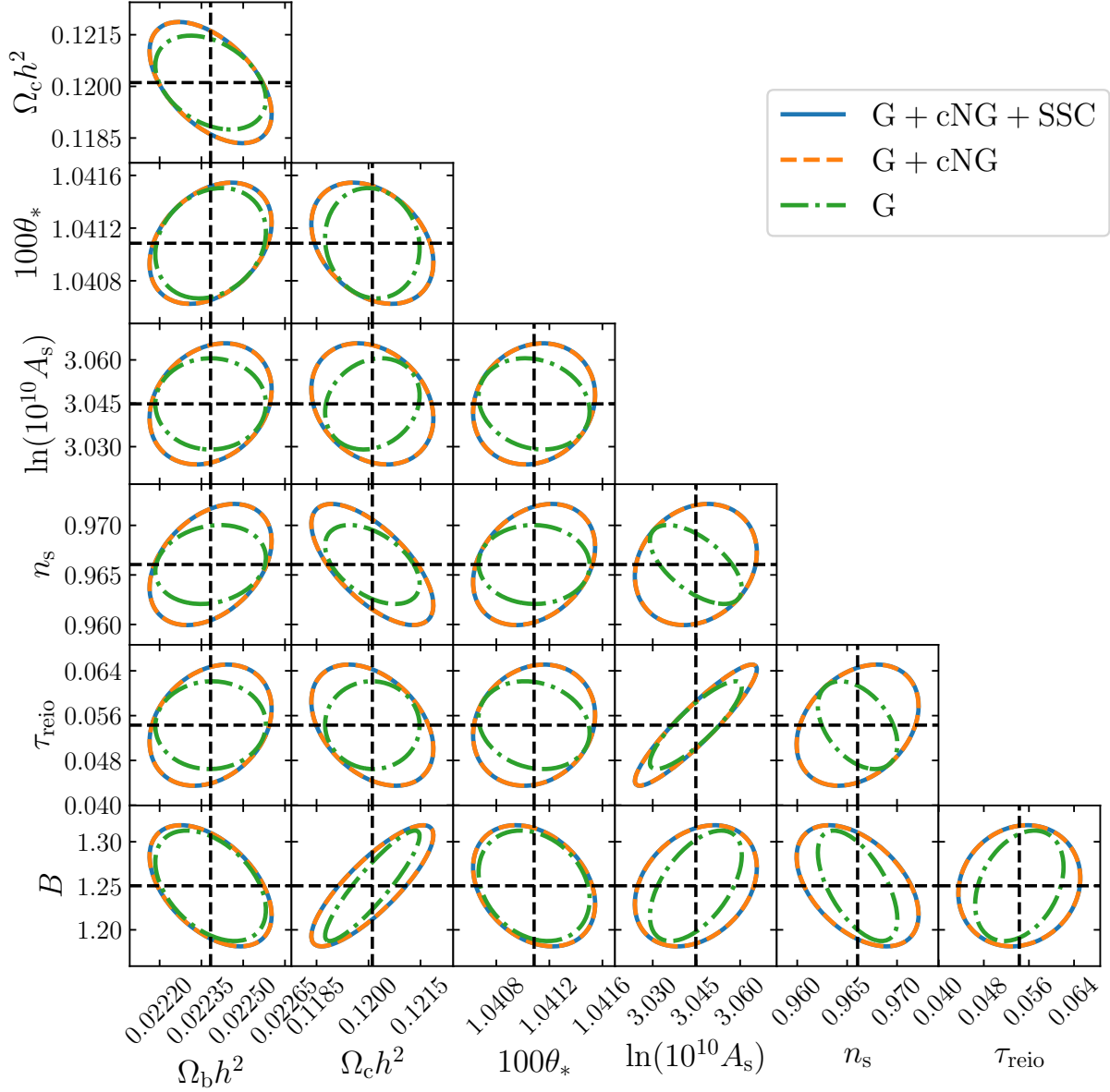


FIG. 8. The expected  $1\text{-}\sigma$  constraints on parameters including marginalization over other parameters, obtained based on the Fisher matrix (see text for details). The cluster masking is not applied. The blue solid, orange dashed, and green dot-dashed lines correspond to the results with total, Gaussian and connected non-Gaussian, Gaussian only covariances, respectively.

- Page, L. Parker, S. T. Staggs, O. Stryzak, E. R. Switzer, R. Thornton, C. Tucker, E. Wollack, and Y. Zhao, *Astrophys. J. Suppl.* **194**, 41 (2011), arXiv:1007.0290 [astro-ph.IM].
- [14] J. Dunkley, R. Hlozek, J. Sievers, V. Acquaviva, P. A. R. Ade, P. Aguirre, M. Amiri, J. W. Appel, L. F. Barrientos, E. S. Battistelli, J. R. Bond, B. Brown, B. Burger, J. Chervenak, S. Das, M. J. Devlin, S. R. Dicker, W. Bertrand Doriese, R. Dünner, T. Essinger-Hileman,

R. P. Fisher, J. W. Fowler, A. Hajian, M. Halpern, M. Hasselfield, C. Hernández-Monteagudo, G. C. Hilton, M. Hilton, A. D. Hincks, K. M. Huffenberger, D. H. Hughes, J. P. Hughes, L. Infante, K. D. Irwin, J. B. Juin, M. Kaul, J. Klein, A. Kosowsky, J. M. Lau, M. Limon, Y. T. Lin, R. H. Lupton, T. A. Marriage, D. Marsden, P. Matuskopf, F. Menanteau, K. Moodley, H. Moseley, C. B. Netterfield, M. D. Niemack, M. R. Nolta, L. A. Page, L. Parker, B. Partridge, B. Reid, N. Se-

# With cluster masking

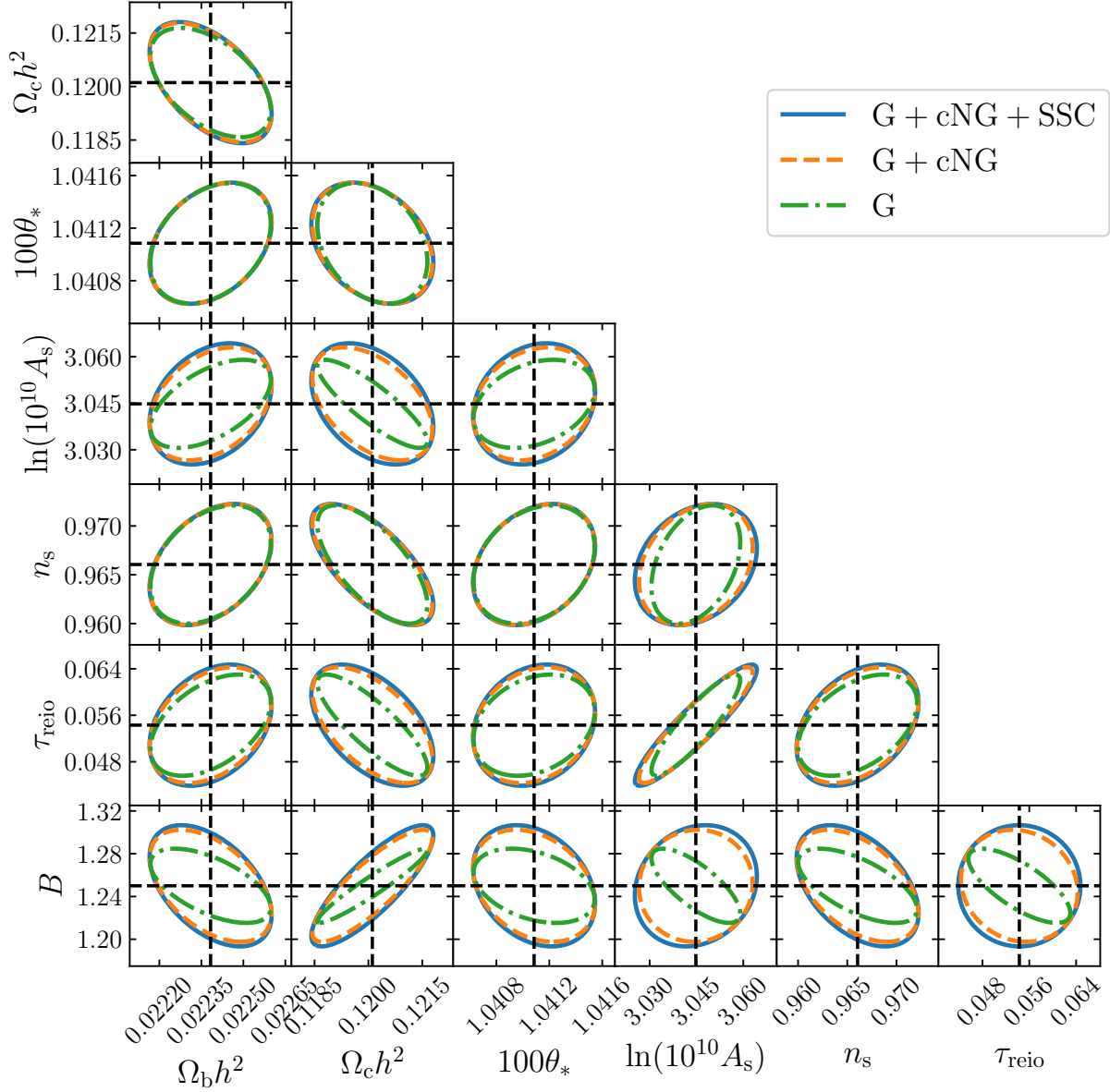


FIG. 9. Similar to the previous figure, but the expected constraints when the cluster masking is applied. The blue solid, orange dashed, and green dot-dashed lines correspond to the results with total, Gaussian and connected non-Gaussian, Gaussian only covariances, respectively.

- hgal, B. Sherwin, D. N. Spergel, S. T. Staggs, D. S. Swetz, E. R. Switzer, R. Thornton, H. Trac, C. Tucker, R. Warne, E. Wollack, and Y. Zhao, *Astrophys. J.* **739**, 52 (2011), arXiv:1009.0866 [astro-ph.CO].
- [15] B. A. Benson, P. A. R. Ade, Z. Ahmed, S. W. Allen, K. Arnold, J. E. Austermann, A. N. Bender, L. E. Bleem, J. E. Carlstrom, C. L. Chang, H. M. Cho, J. F. Cliche, T. M. Crawford, A. Cukierman, T. de Haan, M. A. Dobbs, D. Dutcher, W. Everett, A. Gilbert, N. W.

Halverson, D. Hanson, N. L. Harrington, K. Hattori, J. W. Henning, G. C. Hilton, G. P. Holder, W. L. Holzapfel, K. D. Irwin, R. Keisler, L. Knox, D. Kubik, C. L. Kuo, A. T. Lee, E. M. Leitch, D. Li, M. McDonald, S. S. Meyer, J. Montgomery, M. Myers, T. Natoli, H. Nguyen, V. Novosad, S. Padin, Z. Pan, J. Pearson, C. Reichardt, J. E. Ruhl, B. R. Saliwanchik, G. Simard, G. Smecher, J. T. Sayre, E. Shirokoff, A. A. Stark, K. Story, A. Suzuki, K. L. Thompson, C. Tucker, K. Van-

	$\Omega_b h^2$	$\Omega_c h^2$	$100\theta_*$	$\ln(10^{10} A_s)$	$n_s$	$\tau_{\text{reio}}$	$B$
CMB	0.000146	0.00118	0.000307	0.0141	0.00415	0.00730	—
Without cluster masking							
CMB+tSZ (G)	0.000132	0.00090	0.000278	0.0105	0.00264	0.00520	0.0416
CMB+tSZ (G + cNG)	0.000145	0.00117	0.000305	0.0139	0.00404	0.00716	0.0455
CMB+tSZ (G + cNG + SSC)	0.000145	0.00117	0.000305	0.0139	0.00405	0.00717	0.0456
With cluster masking							
CMB+tSZ (G)	0.000142	0.00102	0.000304	0.0094	0.00401	0.00577	0.0230
CMB+tSZ (G + cNG)	0.000144	0.00111	0.000305	0.0121	0.00409	0.00661	0.0347
CMB+tSZ (G + cNG + SSC)	0.000144	0.00113	0.000306	0.0130	0.00411	0.00691	0.0376

TABLE II. The expected  $1-\sigma$  error on each parameter with CMB anisotropies and tSZ power spectrum. We show the values with three different covariances: G, G + cNG, and G + cNG + SSC.

- derlinde, J. D. Vieira, A. Vikhlinin, G. Wang, V. Yefremenko, and K. W. Yoon, in *SPIE*, Society of Photo-Optical Instrumentation Engineers (SPIE) Conference Series, Vol. 9153 (2014) p. 91531P, arXiv:1407.2973 [astro-ph.IM].
- [16] E. M. George, C. L. Reichardt, K. A. Aird, B. A. Benson, L. E. Bleem, J. E. Carlstrom, C. L. Chang, H. M. Cho, T. M. Crawford, A. T. Crites, T. de Haan, M. A. Dobbs, J. Dudley, N. W. Halverson, N. L. Harrington, G. P. Holder, W. L. Holzapfel, Z. Hou, J. D. Hrubes, R. Keisler, L. Knox, A. T. Lee, E. M. Leitch, M. Lueker, D. Luong-Van, J. J. McMahon, J. Mehl, S. S. Meyer, M. Millea, L. M. Mocanu, J. J. Mohr, T. E. Montroy, S. Padin, T. Plagge, C. Pryke, J. E. Ruhl, K. K. Schaffer, L. Shaw, E. Shirokoff, H. G. Spieler, Z. Staniszewski, A. A. Stark, K. T. Story, A. van Engelen, K. Vanderlinde, J. D. Vieira, R. Williamson, and O. Zahn, *Astrophys. J.* **799**, 177 (2015), arXiv:1408.3161 [astro-ph.CO].
- [17] Simons Observatory Collaboration, *J. Cosmol. Astropart. Phys.* **2019**, 056 (2019), arXiv:1808.07445 [astro-ph.CO].
- [18] K. N. Abazajian, P. Adshead, Z. Ahmed, S. W. Allen, D. Alonso, K. S. Arnold, C. Baccigalupi, J. G. Bartlett, N. Battaglia, B. A. Benson, C. A. Bischoff, J. Borrill, V. Buza, E. Calabrese, R. Caldwell, J. E. Carlstrom, C. L. Chang, T. M. Crawford, F.-Y. Cyr-Racine, F. De Bernardis, T. de Haan, S. di Serego Alighieri, J. Dunkley, C. Dvorkin, J. Errard, G. Fabbian, S. Feeney, S. Ferraro, J. P. Filippini, R. Flauger, G. M. Fuller, V. Gluscevic, D. Green, D. Grin, E. Grohs, J. W. Henning, J. C. Hill, R. Hlozek, G. Holder, W. Holzapfel, W. Hu, K. M. Huffenberger, R. Keskitalo, L. Knox, A. Kosowsky, J. Kovac, E. D. Kovetz, C.-L. Kuo, A. Kusaka, M. Le Jeune, A. T. Lee, M. Lilley, M. Loverde, M. S. Madhavacheril, A. Mantz, D. J. E. Marsh, J. McMahon, P. D. Meerburg, J. Meyers, A. D. Miller, J. B. Munoz, H. N. Nguyen, M. D. Niemack, M. Peloso, J. Peloton, L. Pogosian, C. Pryke, M. Raveri, C. L. Reichardt, G. Rocha, A. Rotti, E. Schaan, M. M. Schmittfull, D. Scott, N. Sehgal, S. Shandera, B. D. Sherwin, T. L. Smith, L. Sorbo, G. D. Starkman, K. T. Story, A. van Engelen, J. D. Vieira, S. Watson, N. Whitehorn, and W. L. Kimmy Wu, arXiv e-prints, arXiv:1610.02743 (2016), arXiv:1610.02743 [astro-ph.CO].
- [19] J. C. Hill and E. Pajer, *Phys. Rev. D* **88**, 063526 (2013), arXiv:1303.4726 [astro-ph.CO].
- [20] E. Komatsu and T. Kitayama, *Astrophys. J. Lett.* **526**, L1 (1999), arXiv:astro-ph/9908087 [astro-ph].
- [21] A. Cooray and R. Sheth, *Phys. Rept.* **372**, 1 (2002), arXiv:astro-ph/0206508 [astro-ph].
- [22] L. D. Shaw, D. Nagai, S. Bhattacharya, and E. T. Lau, *Astrophys. J.* **725**, 1452 (2010), arXiv:1006.1945 [astro-ph.CO].
- [23] H. Trac, P. Bode, and J. P. Ostriker, *Astrophys. J.* **727**, 94 (2011), arXiv:1006.2828 [astro-ph.CO].
- [24] I. G. McCarthy, A. M. C. Le Brun, J. Schaye, and G. P. Holder, *Mon. Not. Roy. Astron. Soc.* **440**, 3645 (2014), arXiv:1312.5341 [astro-ph.CO].
- [25] K. Dolag, E. Komatsu, and R. Sunyaev, *Mon. Not. Roy. Astron. Soc.* **463**, 1797 (2016), arXiv:1509.05134 [astro-ph.CO].
- [26] B. Bolliet, B. Comis, E. Komatsu, and J. F. Macías-Pérez, *Mon. Not. Roy. Astron. Soc.* **477**, 4957 (2018), arXiv:1712.00788 [astro-ph.CO].
- [27] W. Fang, K. Kadota, and M. Takada, *Phys. Rev. D* **85**, 023007 (2012), arXiv:1109.4934 [astro-ph.CO].
- [28] L. Van Waerbeke, G. Hinshaw, and N. Murray, *Phys. Rev. D* **89**, 023508 (2014), arXiv:1310.5721 [astro-ph.CO].
- [29] N. Battaglia, J. C. Hill, and N. Murray, *Astrophys. J.* **812**, 154 (2015), arXiv:1412.5593 [astro-ph.CO].
- [30] A. Hojjati, T. Tröster, J. Harnois-Déraps, I. G. McCarthy, L. van Waerbeke, A. Choi, T. Erben, C. Heymans, H. Hildebrandt, G. Hinshaw, Y.-Z. Ma, L. Miller, M. Viola, and H. Tanimura, *Mon. Not. Roy. Astron. Soc.* **471**, 1565 (2017), arXiv:1608.07581 [astro-ph.CO].
- [31] K. Osato, S. Flender, D. Nagai, M. Shirasaki, and N. Yoshida, *Mon. Not. Roy. Astron. Soc.* **475**, 532 (2018), arXiv:1706.08972 [astro-ph.CO].
- [32] R. Makiya, S. Ando, and E. Komatsu, *Mon. Not. Roy. Astron. Soc.* **480**, 3928 (2018), arXiv:1804.05008 [astro-ph.CO].
- [33] K. Osato, M. Shirasaki, H. Miyatake, D. Nagai, N. Yoshida, M. Oguri, and R. Takahashi, *Mon. Not. Roy. Astron. Soc.* **492**, 4780 (2020), arXiv:1910.07526 [astro-ph.CO].
- [34] R. Makiya, C. Hikage, and E. Komatsu, *Publ. Astron. Soc. Jpn.* **72**, 26 (2020), arXiv:1907.07870 [astro-ph.CO].
- [35] M. Takada and W. Hu, *Phys. Rev. D* **87**, 123504 (2013), arXiv:1302.6994 [astro-ph.CO].

- [36] B. Horowitz and U. Seljak, *Mon. Not. Roy. Astron. Soc.* **469**, 394 (2017), arXiv:1609.01850 [astro-ph.CO].
- [37] L. D. Shaw, O. Zahn, G. P. Holder, and O. Doré, *Astrophys. J.* **702**, 368 (2009), arXiv:0903.5322 [astro-ph.CO].
- [38] Planck Collaboration, *Astron. Astrophys.* **641**, A1 (2020), arXiv:1807.06205 [astro-ph.CO].
- [39] Planck Collaboration, *Astron. Astrophys.* **641**, A6 (2020), arXiv:1807.06209 [astro-ph.CO].
- [40] The comoving distance also serve as the indicator of the cosmic time.
- [41] D. Blas, J. Lesgourgues, and T. Tram, *J. Cosmol. Astropart. Phys.* **2011**, 034 (2011), arXiv:1104.2933 [astro-ph.CO].
- [42] G. L. Bryan and M. L. Norman, *Astrophys. J.* **495**, 80 (1998), arXiv:astro-ph/9710107 [astro-ph].
- [43] J. F. Navarro, C. S. Frenk, and S. D. M. White, *Astrophys. J.* **462**, 563 (1996), arXiv:astro-ph/9508025 [astro-ph].
- [44] J. F. Navarro, C. S. Frenk, and S. D. M. White, *Astrophys. J.* **490**, 493 (1997), arXiv:astro-ph/9611107 [astro-ph].
- [45] A. Klypin, G. Yepes, S. Gottlöber, F. Prada, and S. Heß, *Mon. Not. Roy. Astron. Soc.* **457**, 4340 (2016), arXiv:1411.4001 [astro-ph.CO].
- [46] S. Bocquet, A. Saro, K. Dolag, and J. J. Mohr, *Mon. Not. Roy. Astron. Soc.* **456**, 2361 (2016), arXiv:1502.07357 [astro-ph.CO].
- [47] J. L. Tinker, B. E. Robertson, A. V. Kravtsov, A. Klypin, M. S. Warren, G. Yepes, and S. Gottlöber, *Astrophys. J.* **724**, 878 (2010), arXiv:1001.3162 [astro-ph.CO].
- [48] D. Nagai, A. V. Kravtsov, and A. Vikhlinin, *Astrophys. J.* **668**, 1 (2007), arXiv:astro-ph/0703661 [astro-ph].
- [49] Planck Collaboration, *Astron. Astrophys.* **550**, A131 (2013), arXiv:1207.4061 [astro-ph.CO].
- [50] D. Suto, H. Kawahara, T. Kitayama, S. Sasaki, Y. Suto, and R. Cen, *Astrophys. J.* **767**, 79 (2013), arXiv:1302.5172 [astro-ph.CO].
- [51] K. Nelson, E. T. Lau, and D. Nagai, *Astrophys. J.* **792**, 25 (2014), arXiv:1404.4636 [astro-ph.CO].
- [52] X. Shi, E. Komatsu, K. Nelson, and D. Nagai, *Mon. Not. Roy. Astron. Soc.* **448**, 1020 (2015), arXiv:1408.3832 [astro-ph.CO].
- [53] F. Vazza, M. Angelinelli, T. W. Jones, D. Eckert, M. Brüggen, G. Brunetti, and C. Gheller, *Mon. Not. Roy. Astron. Soc.* **481**, L120 (2018), arXiv:1809.02690 [astro-ph.CO].
- [54] E. Medezinski, N. Battaglia, K. Umetsu, M. Oguri, H. Miyatake, A. J. Nishizawa, C. Sifón, D. N. Spergel, I. N. Chiu, Y.-T. Lin, N. Bahcall, and Y. Komiyama, *Publ. Astron. Soc. Jpn.* **70**, S28 (2018), arXiv:1706.00434 [astro-ph.CO].
- [55] H. Miyatake, N. Battaglia, M. Hilton, E. Medezinski, A. J. Nishizawa, S. More, S. Aiola, N. Bahcall, J. R. Bond, E. Calabrese, S. K. Choi, M. J. Devlin, J. Dunkley, R. Dunner, B. Fuzia, P. Gallardo, M. Gralla, M. Hasselfield, M. Halpern, C. Hikage, J. C. Hill, A. D. Hincks, R. Hložek, K. Huffenberger, J. P. Hughes, B. Koopman, A. Kosowsky, T. Louis, M. S. Madhavacheril, J. McMahon, R. Mandelbaum, T. A. Marriage, L. Maurin, S. Miyazaki, K. Moodley, R. Murata, S. Naess, L. Newburgh, M. D. Niemack, T. Nishimichi, N. Okabe, M. Oguri, K. Osato, L. Page, B. Partridge, N. Robertson, N. Sehgal, B. Sherwin, M. Shirasaki, J. Sievers, C. Sifón, S. Simon, D. N. Spergel, S. T. Staggs, G. Stein, M. Takada, H. Trac, K. Umetsu, A. van Engelen, and E. J. Wollack, *Astrophys. J.* **875**, 63 (2019), arXiv:1804.05873 [astro-ph.CO].
- [56] E. T. Lau, D. Nagai, and K. Nelson, *Astrophys. J.* **777**, 151 (2013), arXiv:1306.3993 [astro-ph.CO].
- [57] In some literature, another definition  $Y'_{500} = Y_{500}/D_A^2$  is employed. In this definition, the unit is normally arcmin<sup>2</sup> and the quantity is computed by integrating observed SZ flux in angular space. For detailed discussions, see Section 3.1 in Ref. [49].
- [58] R. E. Angulo, V. Springel, S. D. M. White, A. Jenkins, C. M. Baugh, and C. S. Frenk, *Mon. Not. Roy. Astron. Soc.* **426**, 2046 (2012), arXiv:1203.3216 [astro-ph.CO].
- [59] A. Cooray, *Phys. Rev. D* **64**, 063514 (2001), arXiv:astro-ph/0105063 [astro-ph].
- [60] M. Takada and B. Jain, *Mon. Not. Roy. Astron. Soc.* **395**, 2065 (2009), arXiv:0810.4170 [astro-ph].
- [61] M. Sato, T. Hamana, R. Takahashi, M. Takada, N. Yoshida, T. Matsubara, and N. Sugiyama, *Astrophys. J.* **701**, 945 (2009), arXiv:0906.2237 [astro-ph.CO].
- [62] A. J. S. Hamilton, C. D. Rimes, and R. Scoccamarro, *Mon. Not. Roy. Astron. Soc.* **371**, 1188 (2006), arXiv:astro-ph/0511416 [astro-ph].
- [63] M. S. Madhavacheril, J. C. Hill, S. Naess, G. E. Addison, S. Aiola, T. Baidon, N. Battaglia, R. Bean, J. R. Bond, E. Calabrese, V. Calafut, S. K. Choi, O. Darwish, R. Datta, M. J. Devlin, J. Dunkley, R. Dünner, S. Ferraro, P. A. Gallardo, V. Gluscevic, M. Halpern, D. Han, M. Hasselfield, M. Hilton, A. D. Hincks, R. Hložek, S.-P. P. Ho, K. M. Huffenberger, J. P. Hughes, B. J. Koopman, A. Kosowsky, M. Lokken, T. Louis, M. Lungu, A. MacInnis, L. Maurin, J. J. McMahon, K. Moodley, F. Nati, M. D. Niemack, L. A. Page, B. Partridge, N. Robertson, N. Sehgal, E. Schaan, A. Schillaci, B. D. Sherwin, C. Sifón, S. M. Simon, D. N. Spergel, S. T. Staggs, E. R. Storer, A. van Engelen, E. M. Vavagiakis, E. J. Wollack, and Z. Xu, *Phys. Rev. D* **102**, 023534 (2020), arXiv:1911.05717 [astro-ph.CO].
- [64] R. Takahashi, S. Soma, M. Takada, and I. Kayo, *Mon. Not. Roy. Astron. Soc.* **444**, 3473 (2014), arXiv:1405.2666 [astro-ph.CO].
- [65] M. Tegmark, A. N. Taylor, and A. F. Heavens, *Astrophys. J.* **480**, 22 (1997), arXiv:astro-ph/9603021 [astro-ph].
- [66] M. Tegmark, *Phys. Rev. Lett.* **79**, 3806 (1997), arXiv:astro-ph/9706198 [astro-ph].
- [67] M. Takada and D. N. Spergel, *Mon. Not. Roy. Astron. Soc.* **441**, 2456 (2014), arXiv:1307.4399 [astro-ph.CO].
- [68] E. Schaan, M. Takada, and D. N. Spergel, *Phys. Rev. D* **90**, 123523 (2014), arXiv:1406.3330 [astro-ph.CO].